JOURNAL OF PROPULSION AND POWER
Vol. 9, No. 3, May–June 1993

Multipassage Three-Dimensional Navier-Stokes Simulation of Turbine Rotor-Stator Interaction

N. K. Madavan* and M. M. Rai†
NASA Ames Research Center, Moffett Field, California 94035
and
S. Gavali‡
Fujitsu America, Inc., San Jose, California 95134

This article deals with the development and validation of a three-dimensional, multipassage, Navier-Stokes code for predicting the unsteady effects due to rotor-stator interaction in turbomachines. Prior work in two dimensions has demonstrated the necessity of including multiple rotor and stator passages in order to closely approximate the stator-to-rotor airfoil count ratio, and thus accurately predict the unsteady flowfield resulting from rotor-stator interaction. In this article, this multipassage capability is extended to three dimensions. Numerical results obtained from a multipassage (three stator and four rotor passages) calculation of an axial turbine stage are presented. The stator-to-rotor airfoil count ratio (3:4) used in the present calculations is a close approximation to that in the actual turbine configuration (22:28). The numerical results are compared with experimental data wherever possible and to earlier single-passage calculations. The present multipassage approach results in a more accurate computation of the unsteady flowfield than that possible from a single-passage approach.

Introduction

TECHNIQUES for the solution of the unsteady Navier-Stokes equations in the complex passages of turbine or compressor stages have been developed in recent years.[1-13] These techniques consider the turbomachine stage as a complete system (rather than considering individual airfoil rows), and can predict the unsteady effects due to interaction between successive airfoil rows. The development of such unsteady analysis techniques represents a major milestone in the quest for a general predictive capability for flows in turbomachine stages.

This article deals with the techniques developed in Refs. 2–5 for predicting the unsteady effects due to rotor-stator interaction. In Ref. 2, a multiple-zone patched-grid approach was used to simulate the flow past the rotor-stator configuration of an axial turbine. The unsteady, two-dimensional, thin-layer, Navier-Stokes equations were solved in a time-accurate manner to obtain the unsteady flowfield associated with this configuration. The governing equations were solved on a system of patched and overlaid grids with information transfer from one grid to another taking place at the zonal boundaries. The airfoil geometry and flow conditions used were the same as those in Refs. 14–18. A good comparison between the computations and experiment was obtained in the case of time-averaged pressures on the rotor and stator airfoils. Computed surface pressure amplitudes (corresponding to the pressure variation in time) also compared reasonably well with experiment, thus indicating the validity of the computed unsteady component of the flow.

In Refs. 3 and 4 the approximation of two-dimensionality was removed and the complete three-dimensional airfoil geometries were used. In addition, the hub, outer casing, and rotor tip clearance were all included in the calculation. As in Ref. 2, time-averaged airfoil surface pressures were found to compare well with experiment, but numerically obtained pressure amplitudes were only in reasonable agreement with experimental data.

One approximation that was made in obtaining the results of Refs. 2–4 was a rescaling of the geometry of either the rotor or the stator. The experimental turbine configuration of Refs. 14–18 had 22 stator airfoils and 28 rotor airfoils. Therefore, an accurate calculation would require a minimum of 25 airfoils (11 in the stator row and 14 in the rotor row). In order to avoid the computational expense involved in such a simulation, either the rotor or the stator airfoils were rescaled and it was then assumed that the number of airfoils in both the stator and rotor rows were the same. This assumption made it possible to perform a calculation with only one rotor and one stator, thus reducing computation time by more than an order of magnitude. The geometry rescaling is required in order to keep blockage effects the same. For the two-dimensional calculations in Ref. 5, this rescaling had little effect on the time-averaged pressure distribution; its effect on the temporal variations of the flow variables, however, was quite significant. The unsteady results of Ref. 5, obtained using a two-dimensional multipassage calculation that included three stator and four rotor passages, showed considerable improvement over the single-passage results.

This study presents results obtained using a time-accurate, three-dimensional Navier-Stokes code capable of handling multiple stator and rotor passages, and provides further validation of the techniques developed in Refs. 2–5. The two-dimensional calculations described above clearly demonstrated the necessity of using a stator-to-rotor airfoil count ratio that was exactly (or close to) the actual ratio in order to predict accurately the unsteady flowfield resulting from rotor-stator interaction. Numerical results obtained from a multipassage (three stator and four rotor passages) calculation

---

Presented as Paper 91-2464 at the AIAA/SAE/ASME/ASEE 27th Joint Propulsion Conference, Sacramento, CA, June 24–26, 1991; received July 8, 1991; revision received June 30, 1992; accepted for publication Nov. 30, 1992.

*Senior Research Scientist, MCAT Institute, M/S 202A-2. Senior Member AIAA.

†Senior Staff Scientist, Fluid Dynamics Division, M/S 258-1. Associate Fellow AIAA.

‡Senior Applications Analyst, Supercomputer Group, 3055 Orchard Drive.

of an axial turbine stage are presented in this study. The stator-to-rotor airfoil count ratio (3:4, i.e., 21:28) used in the present calculations is a close approximation to that in the actual turbine configuration (22:28). This results in a more accurate prediction of the unsteady flowfield than that possible from a single-passage calculation (where the airfoil count ratio is assumed to be unity). The numerical results are compared with experimental data, wherever possible, and to earlier single-passage calculations. In addition, the rotor tip clearance region is modeled more accurately than in previous investigations. The calculations have resulted in a comprehensive description of the flowfield in the single-stage axial turbine of Refs. 14–18; some representative results depicting this flowfield are presented here.

The following sections briefly describe the grids used in the calculation, the numerical methodology, and the various boundary conditions employed. Hub-to-tip variations of time-averaged pressures and pressure amplitudes (corresponding to temporal pressure fluctuations) predicted by the multipassage calculations are presented and compared with earlier single-passage predictions[4] and with experimental results where available. Plots of limiting streamlines showing the influence of the endwall secondary flow vortices are also included and compared with experimental data.

Turbine Geometry and Flowfield Discretization

The single-stage axial turbine geometry considered here is the same as that used in the experimental investigations of Refs. 14–18. As mentioned earlier, the actual turbine consists of 22 stator airfoils and 28 rotor airfoils. For the multipassage computations reported here, it is assumed that there are 21 stator airfoils instead of 22. (The number of rotor airfoils is not changed.) This assumption allows a three-stator/four-rotor airfoil combination to be simulated, with the remaining airfoils being accounted for through periodicity conditions. To properly account for blockage effects, the stator geometry is scaled up by a factor 22/21, keeping the pitch-to-chord ratio constant. This scaling factor is quite small when compared with the scaling factor of 22/28 used in the single-passage computations.[4] This rescaling strategy in effect alters the aspect ratio of the stator airfoil. For the single-passage computations, the stator airfoil aspect ratio is increased by 28/22, whereas for the multipassage computations it is reduced by 21/22. Figure 1 is a perspective view of the rotor-stator configuration considered here with the outer casing removed.

A multiple-zone grid is used to discretize the turbine flowfield. The complete three-dimensional grid consists of a sequence of two-dimensional grids that are stacked together in the radial direction (from hub to tip). The two-dimensional grids at each radial location are similar (except in the tip clearance area). Figure 2 shows the grid at the midspan location. The regions surrounding the airfoils are discretized using "O" grids (inner zones). These inner zones are overlaid onto their respective outer zones that are discretized using "H" grids. The stator inner and outer zones are both stationary, while the rotor zones rotate with the rotor. Note that the outer zones of the rotor and stator airfoils also overlap each other. Information transfer between the various zones is effected through interface boundary conditions at the zone boundaries.

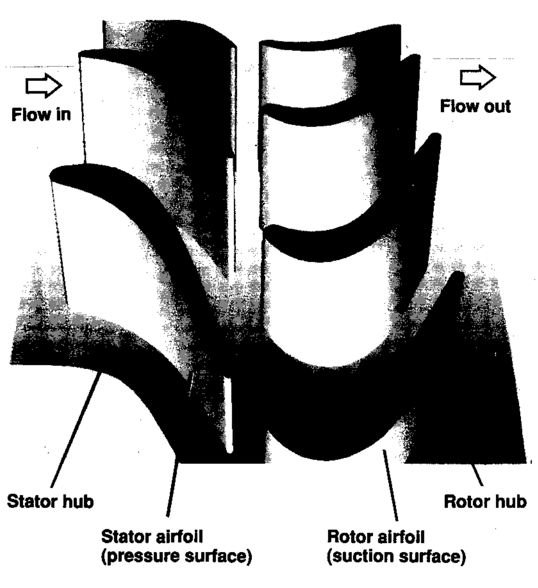

Fig. 1 Perspective view of the rotor-stator geometry considered in the multipassage computations.

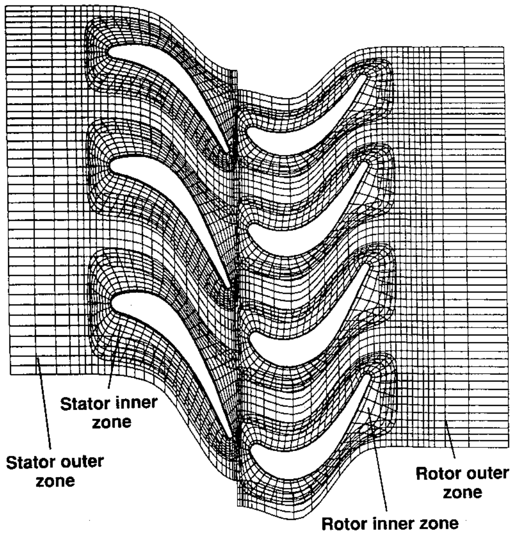

Fig. 2 Computational grid at the midspan location for the multipassage computations.

All the zones in Fig. 2 lie on a cylinder of constant radius, leading to two-dimensional zonal boundaries; this reduces interface logic considerably. Note also that, for the purpose of clarity, Fig. 2 does not show all the grid points used in the calculation.

In the tip clearance region, additional grids are provided interior to the rotor airfoils. These are essentially O grids, with the innermost O grid lines collapsing into double-valued curves. Again, several of these interior grids are stacked in the radial direction to form the grid in the tip clearance area of each rotor airfoil. Note that the stator airfoils, on the other hand, do not require such interior grids since they extend all the way from the hub to the outer casting.

The grid points are densely packed close to the airfoil surfaces in the inner zones to resolve the viscous effects. The stacking of the two-dimensional grids in the radial (spanwise) direction reflects the presence of the hub and tip boundary layers; the two-dimensional grids are densely packed near the hub and outer casing. At each radial location the inner grid around each airfoil contained 2121 points (101 × 21), and the outer grid around each airfoil contained approximately 1800 grid points (58 × 31) and (60 × 31). The interior rotor grid contained 1111 grid points (101 × 11). In the radial direction, 51 two-dimensional grids were stacked together, with the last 10 corresponding to the rotor tip clearance. The total number of grid points used was 1.43 million. This is in contrast to the 0.41 million grid points used in the single-passage computations.[4]

Numerical Methodology

The unsteady, thin-layer Navier-Stokes equations in three spatial dimensions are solved using an upwind-biased finite-difference algorithm. This algorithm is third-order accurate in space and second-order accurate in time. It is set in an iterative, factored, implicit framework in which several iterations are performed at each time-step so that the fully implicit finite-difference equations are solved. In this scheme, factorization and linearization errors can be driven to zero at each step. Details regarding the method can be found in Refs. 2–5 and are omitted here for brevity.

Boundary conditions at the various natural boundaries of the flow domain are implemented in an implicit manner within the framework of the iterative scheme. Subsonic inflow and outflow boundary conditions are imposed at the stator inlet and rotor exit, respectively. At the stator inlet, four quantities (a Riemann invariant, the entropy, and the radial and tangential flow velocities) are prescribed while the fifth quantity (also a Riemann invariant) is extrapolated from the interior of the solution domain. At the rotor exit, only one quantity needs to be specified; the other four quantities can be extrapolated from the interior. Here, a constant pressure is imposed at midspan at the rotor exit. The pressures at all other radial locations at the rotor exit are obtained from the radial equilibrium condition. Periodicity boundary conditions are imposed on the upper and lower boundaries (Fig. 2), over a composite three-stator (or four-rotor) pitch. No-slip, adiabatic wall, and zero normal pressure derivative conditions are imposed on the airfoil surfaces and on the hub and outer casing.

In addition to the above, the use of a zonal approach results in several zonal boundaries where boundary conditions must be prescribed. In the interest of brevity, the implementation of these zonal boundary conditions is not discussed here. Details may be found in Refs. 2 and 3 and the references cited therein.

Results

The results obtained for the multipassage computations of the rotor-stator configuration shown in Fig. 1 are presented in this section and compared with earlier single-passage computations[4] and experimental results. The results were obtained by integrating the governing equations and the boundary conditions described earlier. Four iterations of the iterative algorithm were performed at each step. Approximately five rotor cycles (a rotor cycle corresponds to the motion of the rotor through an angle equal to $2\pi/N$, where N is the number of rotor airfoils) were required to eliminate the initial transients and establish a solution that was periodic in time. The results of earlier single-passage computations were used to provide a starting solution for the present computations. All calculations were performed at a constant time-step value of about 0.08 (this translates into 1000 time steps per cycle). Each cycle required about 72 h single-processor CPU time on the NASA Ames Cray YMP8/832.

A modified version of the Baldwin-Lomax turbulence model[19,20] was used to determine the eddy viscosity. The kinematic viscosity was calculated using Sutherland's law. The inlet Mach number used for the calculation was 0.07, the flow coefficient was 0.78, and the Reynolds number was 100,000/in.

Time-Averaged Pressures

Figures 3a–c and Figs. 4a–c show the predicted and experimental time-averaged pressure coefficient C_p as a function of the nondimensional axial distance at various spanwise locations for the stator and rotor airfoils, respectively. The pressure coefficient is defined as

$$C_p = [(p_{\text{avg}} - p_{t_i})/\tfrac{1}{2}\rho_i\omega^2]$$

where p_{avg} is the static pressure averaged over one stator (or rotor) cycle, p_{t_i} and ρ_i are the average total pressure and density, respectively at midspan at the inlet, and ω is the velocity of the rotor at midspan. The axial distance is nondimensionalized by the axial chord. In Fig. 3 (and in subsequent figures) the dashed lines represent the single-passage results while the solid lines represent the multipassage results.

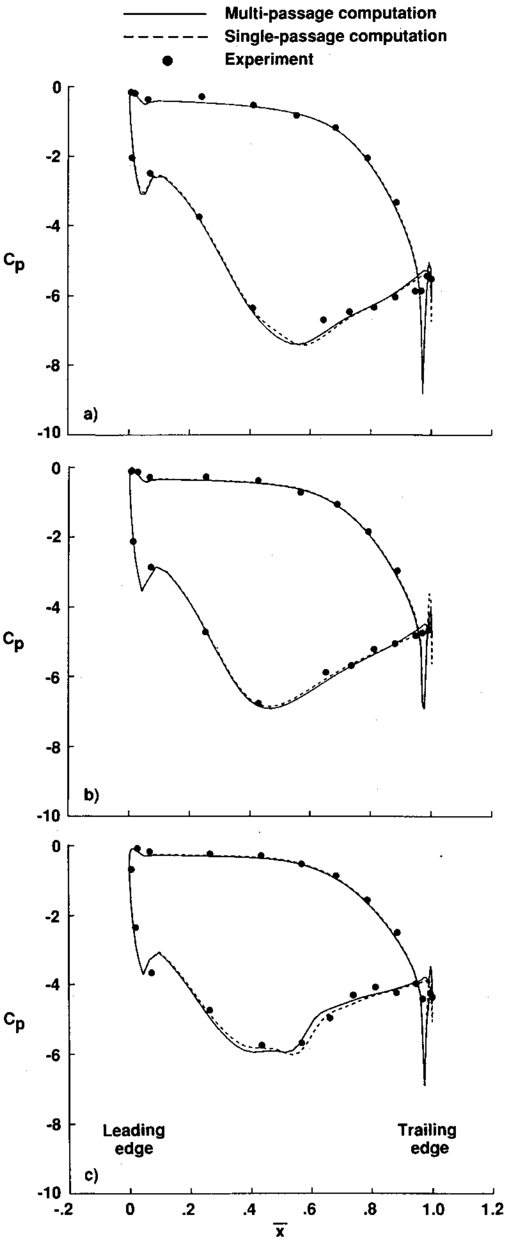

Fig. 3 Spanwise variation of time-averaged pressure distributions on the stator: a) 2% span, b) 50% span, and c) 98% span.

It must be noted that the experimental data presented in these figures were obtained with an axial gap of 50%,[14] whereas the numerical data were obtained with an axial gap of 15%. However, the results[14] indicate that for this turbine configuration the axial gap has negligible effect on time-averaged stator surface pressures, and at most a weak effect on time-averaged rotor surface pressures. Hence, the following comparisons between computations and experiment are valid.

Figures 3a–d show experimental and numerical C_p distributions on the stator at 2, 50, and 98% of the span, respectively. In general, the comparison between the computations and experiment is good. Additionally, the results from the single- and multipassage calculations agree well with each other. Both calculations predict a small separation bubble (seen as a spatial fluctuation in pressure) at the trailing edge.

Figures 4a–c show the time-averaged C_p distributions on the rotor airfoil at 2, 50, and 98% of the span, respectively. The increasing effect of the tip-leakage vortex on the rotor surface pressures in the region close to the rotor tip is evident from the lower pressure values at about 70% chord (Fig. 4c) on the suction side. Figures 4a–c show reasonable agreement

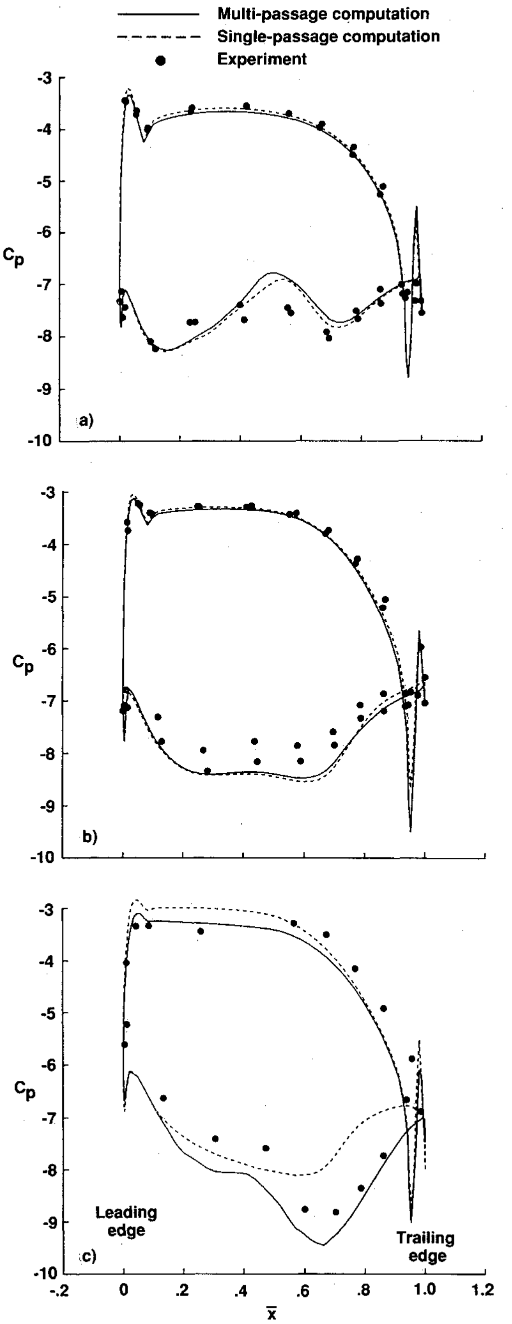

Fig. 4 Spanwise variation of time-averaged pressure distributions on the rotor: a) 2% span, b) 50% span, and c) 98% span.

between the numerical results and the experimental data. The major difference between the single- and multipassage computation is in Fig. 4c, where the multipassage results show closer agreement with the experiment. This is because the tip clearance region is properly accounted for in the present computation; the single-passage computation used a much smaller tip clearance (0.4% of span) than in the experiment (1% of span).

Thus, in general, the time-averaged pressures obtained from the single- and multipassage calculations are almost identical, except in the vicinity of the rotor tip clearance region.

Pressure Amplitudes

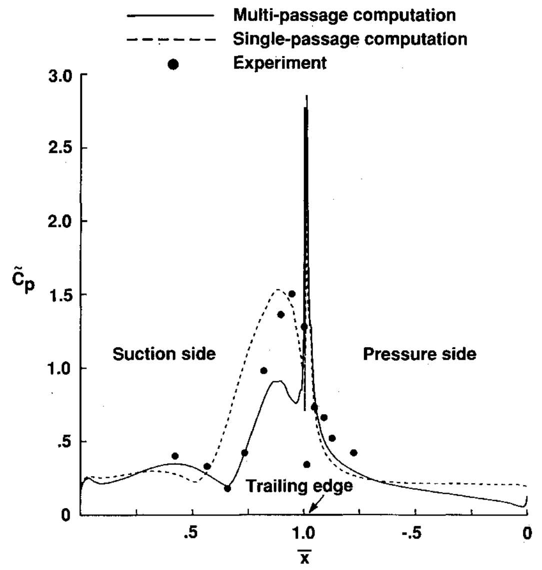

Fig. 5 Pressure amplitude distribution on the stator at midspan.

The amplitude of the temporal pressure fluctuations is a measure of the unsteadiness of the flow. The available experimental data,[14] for an axial gap of 15% average chord, includes pressure amplitudes on the rotor and stator airfoils at the midspan location. Figure 5 shows pressure amplitudes $\tilde{C}_p$ on the surface of the stator plotted as a function of the nondimensional axial distance. The quantity $\tilde{C}_p$ is defined as

$$\tilde{C}_p = [(p_{\max} - p_{\min})/\tfrac{1}{2}\rho_i\omega^2]$$

where $p_{\max}$ and $p_{\min}$ are the maximum and minimum pressures that occur over a cycle at a given point. The single-passage calculations predict a wider large-amplitude region than that found experimentally; the predicted peak is also shifted to the left of the experiment. The multipassage calculations are, however, in much better agreement with the experiment. The predicted location and magnitude of the pressure amplitude minimum on the suction side agrees well with the experiment; the extent of the large amplitude region around the stator trailing edge also agrees well with the experiment. The only discrepancy is in the level of the peak amplitude which is probably related to the grid resolution.

The improved results with the multipassage calculation stem directly from the fact that the stator-to-rotor airfoil count closely matches that of the experimental turbine. In addition, for the actual turbine, with a stator-to-rotor airfoil count ratio of 22:28, it can be shown from a simple acoustic analysis[21] that only the higher harmonics in time give rise to propagating waves, the lower harmonics give rise to decaying signals. When the single-passage approximation is made, a similar analysis shows that every harmonic in time results in a propagating wave in the axial direction. These relatively large calculated pressure waves are reflected by the exit boundary and distort the unsteady pressures everywhere.

Figure 6 shows the $\tilde{C}_p$ distribution on the rotor. The agreement between the multipassage results and experiment is much better than with the single-passage results. Both the location and magnitude of the suction side amplitude peak is well-predicted. It is interesting to note that earlier two-dimensional calculations[5] of this turbine configuration, with the same 3:4 stator-to-rotor airfoil count ratio, did not result in similar agreement with experiment in terms of the rotor pressure amplitudes. Furthermore, two-dimensional calculations (unpublished), with the exact stator-to-rotor airfoil count ratio of 11:14, did not show any improvement over the above. Thus, the agreement between the present results and experiment is due to a combination of including three-dimensionality and the multipassage approach.

Time-Averaged Limiting Streamlines

The nature of the flow close to the surfaces of the rotor and stator airfoils and the hub surface can be better understood from the pattern of limiting streamlines on these sur-

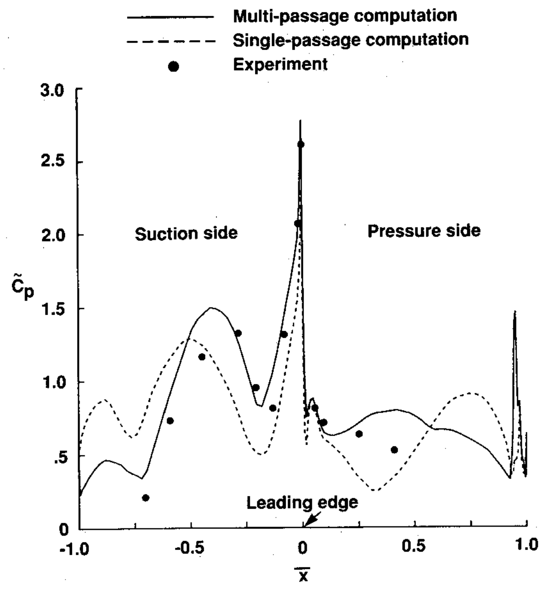

Fig. 6 Pressure amplitude distribution on the rotor at midspan.

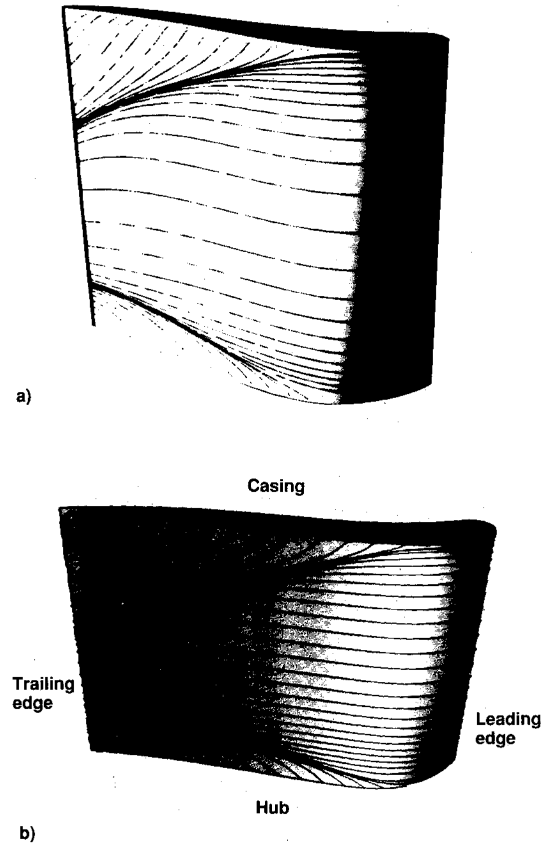

Fig. 7 Stator suction surface flow visualization. Time-averaged limiting streamlines from a) single-passage computations, and b) multipassage computations.

faces. The results presented here were obtained by releasing particles on the grid surface just above the airfoil surface and then tracking these particles as they were convected by the time-averaged velocity field. The motion of the particles was restricted to the grid surface on which they were originally released (i.e., the out-of-surface component of velocity was not used to move the particle).

The limiting streamlines on the stator pressure surface obtained from the multipassage computations were nearly identical to those obtained from the single-passage computations[4] and are therefore not shown here. The flow was noted to be two-dimensional nearly everywhere except in a small region near the endwalls in the vicinity of the leading edge (where the incoming boundary layer separates and forms a horseshoe vortex).

The limiting streamlines on the stator suction surface are compared in Figs. 7a and 7b. In both figures, the upward motion of the fluid particles near the hub (0–15% span) is caused by the hub secondary flow vortex generated by the neighboring stator airfoil. The upper half of the figures is qualitatively a mirror image of the lower half. The secondary flow vortex associated with the casing has a sense of rotation that is opposite to that of the hub secondary flow vortex. Therefore, it induces a radially inward flow on the stator suction surface that extends almost all the way to midspan. The casing secondary flow vortex, just like the hub secondary flow vortex, is pulled toward the hub because it contains low total pressure fluid. However, unlike the hub secondary flow vortex which gets confined to the hub region because of its downward motion, the casing secondary flow vortex gets elongated, and thus affects a greater portion of the stator surface. The midspan flow on the suction side is largely two-dimensional.

Figures 8a and 8b show limiting streamlines on the rotor airfoil pressure surface. Both figures show a strong radial

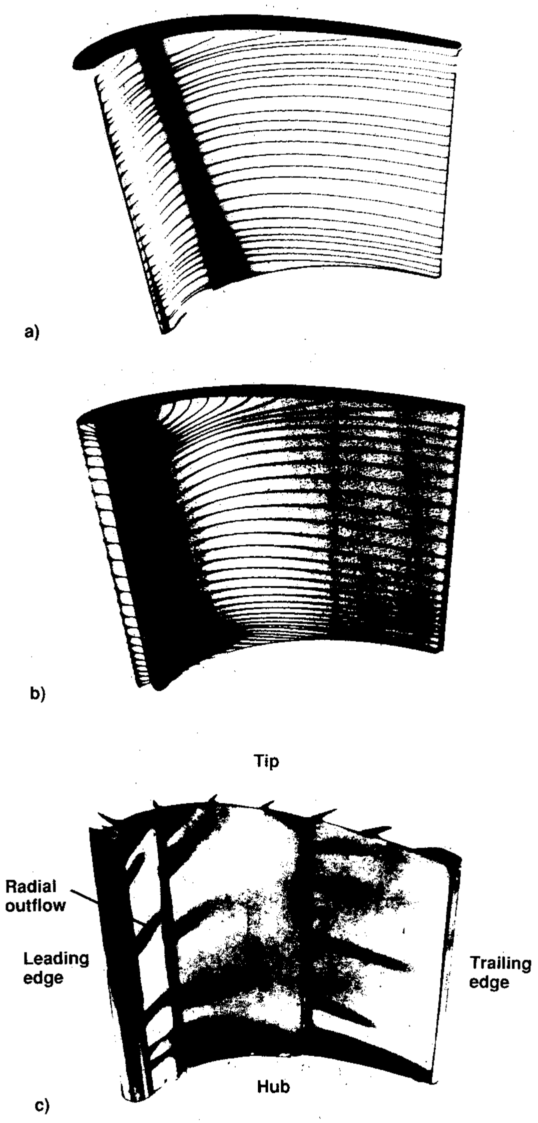

Fig. 8 Rotor pressure surface flow visualization: a) time-averaged limiting streamlines from single-passage computations, b) time-averaged limiting streamlines from multipassage computations, and c) experimental results.

outflow in the first 30% of the chord from the leading edge due to the "relative-eddy" effect.[16] Beyond this, the flow is almost two-dimensional. Experimental flow visualization results[17] are shown in Fig. 8c for comparison. In general, there is good qualitative agreement between the numerical results of Figs. 8a and 8b, and the experimental data of Fig. 8c. However, the multipassage results shown in Fig. 8b are in better agreement with the experiment.

The rotor suction surface limiting streamlines are shown in Figs. 9a and 9b. It is only in these figures that marked differences between the single- (Fig. 9a) and multipassage (Fig. 9b) calculations are noted. As in the case of the stator, the endwall secondary flows induce strong radial components in the surface velocity field. Both figures clearly show the two lines of separation caused by the endwall secondary flow vortices, the two separation lines move toward each other and the midspan region. In the multipassage results, an additional line of separation caused by the tip leakage flow can also be seen. There is also evidence of the interaction between the casing secondary flow vortex and the leakage flow in the aft portion of the rotor in Fig. 9b. Although these features do not appear in Fig. 9a, a close examination of the single-passage results also revealed a similar line of separation very close to the rotor tip. Since the tip clearance in the single-passage calculation was much smaller, the leakage vortex was weaker and did not interact with the casing or hub secondary flow vortices. Experimental flow visualization results are shown in Fig. 9c. In general, results from both the single- and multipassage computations agree qualitatively with experiment. However, detailed features predicted by the present calculation (Fig. 9b) of the tip leakage flow and the flow in the aft portion of the rotor airfoil cannot be clearly discerned from the experiment.

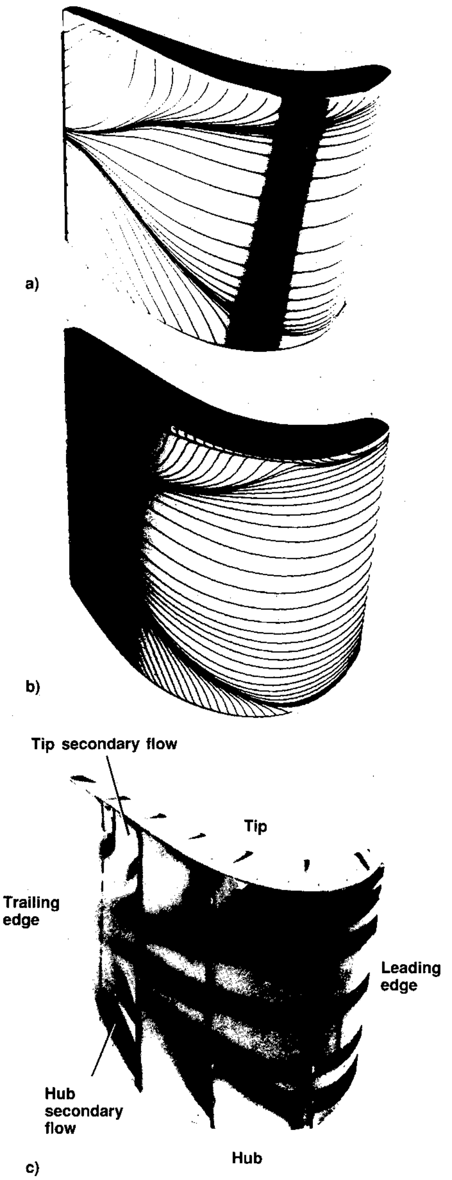

Fig. 9 Rotor suction surface flow visualization: a) time-averaged limiting streamlines from single-passage computations, b) time-averaged limiting streamlines from multipassage computations, and c) experimental results.

Total Pressure Contours at the Exit to the Stator and Rotor

A better understanding of the endwall secondary flow structure can be obtained from contours of total pressure at the exits to the stator and the rotor. The endwall secondary flow vortices contain fluid from the endwall boundary layers and the airfoil surface boundary layers and, therefore, represent low total pressure regions (compared with freestream total pressure values). The difference in vortex total pressures and freestream total pressure enables one to clearly observe secondary flow vortex structure by studying total pressure contours at appropriate locations.

Figures 10a–c compare the time-averaged total pressure contours, in the absolute frame of reference, at the exit to the stator (8.8% of the stator chord downstream of stator

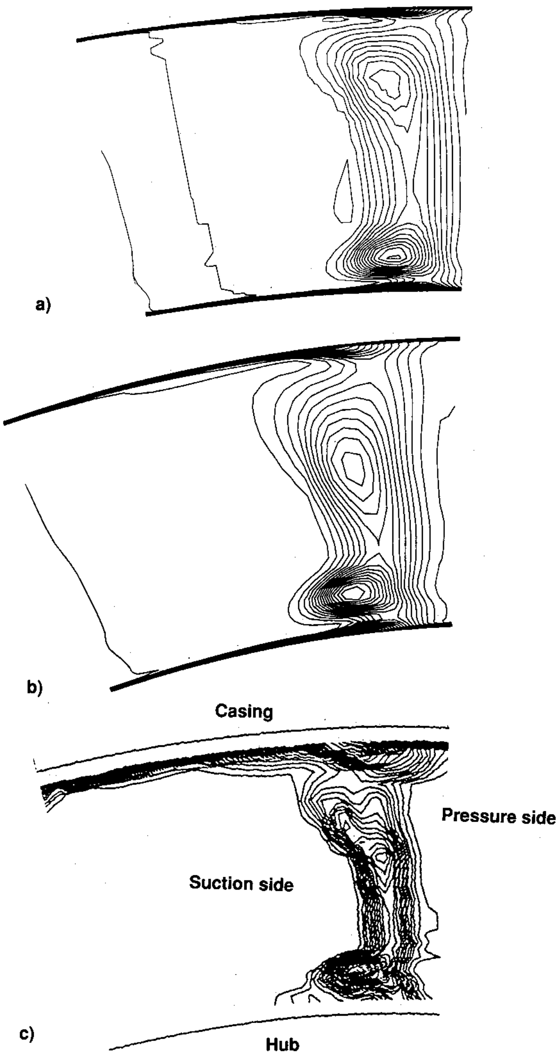

Fig. 10 Absolute total pressure contours at the exit to the stator: a) single-passage computations, b) multipassage computations, and c) experimental results.

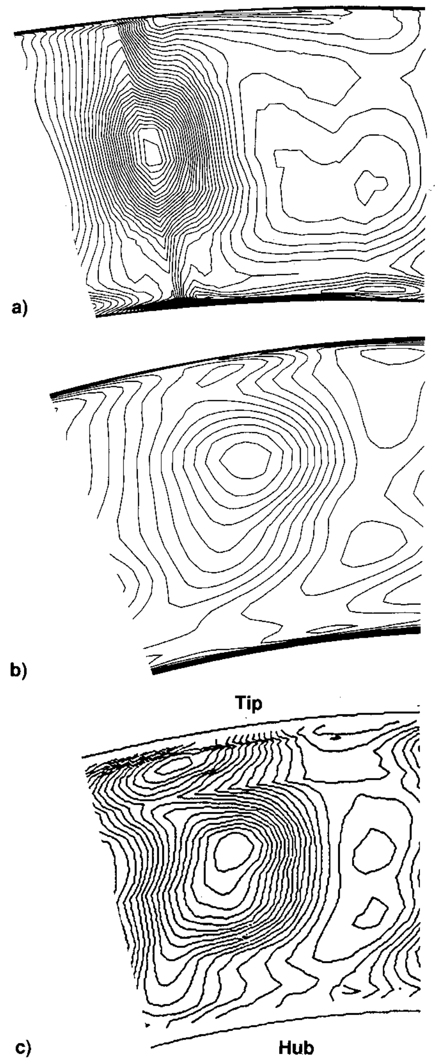

Fig. 11 Relative total pressure contours at the exit to the rotor: a) single-passage computations, b) multipassage computations, and c) experimental results.

trailing edge). Figure 10a presents results from the single-passage calculation, while Fig. 10b presents results from the multipassage calculation. Three distinct entities are clearly seen in the figures: 1) the hub secondary flow vortex, 2) the casing secondary flow vortex, and 3) the stator wake. The hub secondary flow vortex is seen to be confined to a region close to the hub. The casing secondary flow vortex is elongated and occupies a relatively larger portion of the span; the location of the vortex core is further away from the casing for the multipassage calculations and agrees better with the experimental results shown in Fig. 10c. Note that Figs. 10a and 10b also show the endwall boundary layers in the form of highly clustered total pressure contours at the lower and upper boundaries.

Time-averaged relative total pressure contours downstream of the rotor (at a location 36% chord aft of the rotor trailing edge) are presented in Figs. 11a and 11b for the single- and multipassage calculations, respectively; experimental results are presented in Fig. 11c. The endwall secondary flow vortices appear to have merged into a single low total pressure region with its center at about 60% span. Overall, there is better agreement between the multipassage and experimental results. Clearly, the tip leakage vortex structure predicted by the multipassage computation is in close agreement with the experiment. As in the case of the stator exit plane, the endwall boundary layers are also clearly seen at the upper and lower surfaces.

Summary

A three-dimensional, multipassage, Navier-Stokes code has been developed for predicting unsteady turbomachinery flowfields. This code extends the capabilities of the single-passage code developed earlier by allowing the simulation of multiple passages in the stator and rotor airfoil rows. This multipassage capability permits the accurate geometric representation of typical turbomachine stages by including the exact stator-to-rotor airfoil count ratio (or a close approximation to the same). This in turn results in a more accurate computation of the flowfield than that possible with the single-passage approach.

In order to validate the code, a multipassage (three stator and four rotor passage) calculation of an axial turbine stage configuration has been performed. The stator-to-rotor airfoil count ratio (3:4) used in the present calculations is a close approximation to the actual turbine (22:28). In general, the results from the present calculation compare well with experimental data. For the geometry considered here, both the single- and multipassage computations yielded the same time-averaged pressures on the strator and rotor airfoil surfaces. However, as expected, marked differences were noted in the pressure amplitudes predicted by the two computations, with the multipassage computations being in better agreement with the experiment. The small discrepancy between the predicted maximum pressure amplitude on the stator airfoil and experiment is probably a result of inadequate grid resolution; the grid resolution studies required to resolve this discrepancy, however, are currently too expensive to undertake.

Another aspect of the present computation was the use of the correct tip clearance. As a result, better agreement with the experimental time-averaged pressures in the rotor tip region was achieved. In addition, comparisons of surface streamline patterns and endwall secondary flow vortex structure clearly showed better agreement between the multipassage computations and experiment.

The results presented here demonstrate the overall capability of the multipassage code in accurately resolving the various features of the complex, unsteady flowfield in a turbomachine. Such a multipassage approach is crucial to the accurate prediction of more intricate details of the flowfield, such as far-field acoustics and noise.

Acknowledgments

This work was partially funded by the Office of Naval Research. Computer resources were provided under the Numerical Aerodynamic Simulation program. Additional computer resources were provided by Amdahl Corporation, Sunnyvale, California, while S. Gavali was employed there.

References

[1]Erdos, J. I., Alzner, E., and McNally, W., "Numerical Solution of Periodic Transonic Flow Through a Fan Stage," *AIAA Journal*, Vol. 15, No. 11, 1977, pp. 1559–1568.

[2]Rai, M. M., "Navier-Stokes Simulations of Rotor-Stator Interaction Using Patched and Overlaid Grids," *Journal of Propulsion and Power*, Vol. 3, Sept. 1987, pp. 387–396.

[3]Rai, M. M., "Three-Dimensional Navier-Stokes Simulations of Turbine Rotor-Stator Interaction, Part I: Methodology; Part II: Results," *Journal of Propulsion and Power*, Vol. 5, May 1989, pp. 307–319.

[4]Madavan, N. K., Rai, M. M., and Gavali, S., "Grid Refinement Studies of Turbine Rotor-Stator Interaction," AIAA Paper 89-0325, Jan. 1989.

[5]Rai, M. M., and Madavan, N. K., "Multi-Airfoil Navier-Stokes Simulations of Turbine Rotor-Stator Interaction," *Journal of Turbomachinery*, Vol. 112, July 1989, pp. 377–384.

[6]Fourmaux, A., "Unsteady Flow Calculation in Cascades," American Society of Mechanical Engineers Paper 86-GT-178, 1986.

[7]Giles, M. B., "Stator/Rotor Interaction in a Transonic Turbine," *Journal of Propulsion and Power*, Vol. 6, Sept.–Oct. 1990, pp. 621–627.

[8]Lewis, J. P., Delaney, R. A., and Hall, E. J., "Numerical Pre-

diction of Turbine Vane-Blade Interaction," AIAA Paper 87-2149, June 1987.

[9] Jorgenson, P. C. E., and Chima, R. V., "An Explicit Runge-Kutta Method for Unsteady Rotor/Stator Interaction," AIAA Paper 88-0049, Jan. 1988.

[10] Jorgenson, P. C. E., and Chima, R. V., "An Unconditionally Stable Runge-Kutta Method for Unsteady Flows," AIAA Paper 89-0205, Jan. 1989.

[11] Koya, M., and Kotake, S., "Numerical Analysis of Fully Three-Dimensional Periodic Flows Through a Turbine Stage," *Journal of Engineering for Gas Turbines and Power*, Vol. 107, Oct. 1985, pp. 945–952.

[12] Chen, Y. S., "3-D Stator-Rotor Interaction of the SSME," AIAA Paper 88-3095, July 1988.

[13] Gibeling, H. J., Weinberg, B. C., Shamroth, S. J., and McDonald, H., "Flow Through a Compressor Stage," Rept. R86-910004-F, Scientific Research Associates, Glastonbury, CT, May 1986.

[14] Dring, R. P., Joslyn, H. D., Hardin, L. W., and Wagner, J. H., "Turbine Rotor-Stator Interaction," *Journal of Engineering for Power*, Vol. 104, Oct. 1982, pp. 729–742.

[15] Joslyn, H. D., and Dring, R. P., "Three-Dimensional Flow and Temperature Profile Attenuation in an Axial Flow Turbine," Air Force Office of Scientific Research Rept. R89-957334-1, March 1989.

[16] Dring, R. P., and Joslyn, H. D., "The Relative Eddy in Axial Turbine Rotor Passages," American Society of Mechanical Engineers Paper 83-GT-22, 1983.

[17] Dring, R. P., and Joslyn, H. D., "Measurements of Turbine Rotor Blade Flows," *Journal of Engineering for Power*, Vol. 103, April 1981, pp. 400–405.

[18] Sharma, O. P., Butler, T. H., Joslyn, H. D., and Dring, R. P., "Three-Dimensional Unsteady Flow in an Axial Flow Turbine," *Journal of Propulsion and Power*, Vol. 1, Jan.–Feb. 1985, pp. 29–38.

[19] Baldwin, B. S., and Lomax, H., "Thin Layer Approximation and Algebraic Model for Separated Turbulent Flow," AIAA Paper 78-257, Jan. 1978.

[20] Hung, C. M., and Buning, P. G., "Simulation of Blunt-Fin-Induced Shock-Wave and Turbulent Boundary-Layer Interaction," *Journal of Fluid Mechanics*, Vol. 154, May 1985, pp. 163–185.

[21] Tyler, J. M., and Sofrin, T. G., "Axial Flow Compressor Noise Studies," *SAE Transactions*, Vol. 70, 1962, pp. 309–332.

Recommended Reading from Progress in Astronautics and Aeronautics

Dynamics of Deflagrations and Reactive Systems:
Flames - Vol 131 - and Dynamics of Deflagrations and Reactive Systems: Heterogeneous Combustion - Vol 132
A. L. Kuhl, J. C. Leyer, A. A. Borisov, W. A. Sirignano, editors

Companion volumes 131 and 132 in the AIAA Progress in Astronautics and Aeronautics series span a broad area, covering the processes of coupling the exothermic energy release with the fluid dynamics occurring in any combustion process. Contents include: Ignition Dynamics; Diffusion Flames and Shear Effects; Dynamics of Flames and Shear Layers; Turbulent Flames; Flame Propagation in Combustion Engines; Combustion of Dust-Air Mixtures; Droplet Combustion; Combustion At Solid and Liquid Surfaces; Combustion Diagnostics.

1991, 418 pp, illus, Hardback
ISBN 0-930403-95-9
AIAA Members $49.95
Nonmembers $74.95
Order #: V-131 (830)

1991, 386 pp, illus, Hardback
ISBN 0-930403-96-7
AIAA Members $49.95
Nonmembers $74.95
Order #: V-132 (830)

Dynamics of Detonations and Explosions:
Detonations - Vol 133 - and Dynamics of Detonations and Explosions: Explosion Phenomena, Vol 134
A. L. Kuhl, J. C. Leyer, A. A. Borisov, W. A. Sirignano, editors

Companion volumes 133 and 134 in the AIAA Progress in Astronautics and Aeronautics series address the rate processes of energy deposition in a compressible medium and the concurrent nonsteady flow as it typically occurs in explosion phenomena. Contents include: Gaseous Detonations; Detonation: Initiation and Transmission; Nonideal Detonations and Boundary Effects; Multiphase Detonations; Vapor Cloud Explosions; Blast Wave Reflections and Interactions; Vapor Explosions.

1991, 383 pp, illus, Hardback
ISBN 0-930403-97-5
AIAA Members $49.95
Nonmembers $74.95
Order #: V-133 (830)

1991, 408 pp, illus, Hardback
ISBN 0-930403-98-3
AIAA Members $49.95
Nonmembers $74.95
Order #: V-134 (830)

Place your order today! Call 1-800/682-AIAA

AIAA
American Institute of Aeronautics and Astronautics
Publications Customer Service, 9 Jay Gould Ct., P.O. Box 753, Waldorf, MD 20604
Phone 301/645-5643, Dept. 415, FAX 301/843-0159

Sales Tax: CA residents, 8.25%; DC, 6%. For shipping and handling add $4.75 for 1-4 books (call for rates for higher quantities). Orders under $50.00 must be prepaid. Please allow 4 weeks for delivery. Prices are subject to change without notice. Returns will be accepted within 15 days.